



# 2<sup>nd</sup> Advanced Optical Metrology Compendium

## Advanced Optical Metrology

Geoscience | Corrosion | Particles | Additive Manufacturing: Metallurgy, Cut Analysis & Porosity



**EVIDENT**  
**OLYMPUS**

**WILEY**

The latest eBook from **Advanced Optical Metrology**.  
Download for free.

This compendium includes a collection of optical metrology papers, a repository of teaching materials, and instructions on how to publish scientific achievements.

With the aim of improving communication between fundamental research and industrial applications in the field of optical metrology we have collected and organized existing information and made it more accessible and useful for researchers and practitioners.

**EVIDENT**  
**OLYMPUS**

**WILEY**

# Evaluating Phospholipid-Functionalized Gold Nanorods for In Vivo Applications

Lucien Roach, Mary E. Booth, Nicola Ingram, Daniel A. Paterson, Damien V. B. Batchelor, Samuel C. T. Moorcroft, Richard J. Bushby, Kevin Critchley, P. Louise Coletta, and Stephen D. Evans\*

Gold nanorods (AuNRs) have attracted a great deal of attention due to their potential for use in a wide range of biomedical applications. However, their production typically requires the use of the relatively toxic cationic surfactant cetyltrimethylammonium bromide (CTAB) leading to continued demand for protocols to detoxify them for in vivo applications. In this study, a robust and facile protocol for the displacement of CTAB from the surface of AuNRs using phospholipids is presented. After the displacement, CTAB is not detectable by NMR spectroscopy, surface-enhanced Raman spectroscopy, or using pH-dependent  $\zeta$ -potential measurements. The phospholipid functionalized AuNRs demonstrated superior stability and biocompatibility ( $IC_{50} > 200 \mu\text{g mL}^{-1}$ ) compared to both CTAB and polyelectrolyte functionalized AuNRs and are well tolerated in vivo. Furthermore, they have high near-infrared (NIR) absorbance and produce large amounts of heat under NIR illumination, hence such particles are well suited for plasmonic medical applications.

of cancer<sup>[5–7]</sup> and for thermally triggered drug release in the treatment of pathogens.<sup>[8]</sup> AuNPs can be synthesized such that they possess strong absorbance within the “near-infrared biological window.” Within this range of wavelengths, light can penetrate biological tissue by several centimeters. This enables them to be used as in vivo nano-heaters to thermally ablate cancerous tissue with minimal heat generation in the intermediate tissue along the light path.<sup>[9,10]</sup>

In this role, gold nanorods (AuNRs) are exceptionally well suited, offering a strong narrow absorbance peak, tunable throughout red and near-infrared (NIR) wavelengths. While other AuNP morphologies, including nanoplates,<sup>[11]</sup> nanotubes,<sup>[12,13]</sup> and nanoshells<sup>[14]</sup> offer

absorbance peaks in the NIR, AuNRs have the highest absorbance cross-sections ( $\sigma_{\text{abs}}$ ) per unit mass of any AuNP, with an  $\sigma_{\text{abs}}$  typically an order of magnitude higher than that seen for Au nanoshells containing an equivalent mass of Au.<sup>[15]</sup> This is particularly advantageous in photothermal applications as the power of heat generation of an AuNP is proportional to its  $\sigma_{\text{abs}}$  at the illumination wavelength.<sup>[5]</sup>

AuNR synthesis protocols remain dependent on the use of the surfactant cetyltrimethylammonium bromide (CTAB) as a shape-directing agent.<sup>[16–18]</sup> This is problematic as CTAB is a highly toxic amphiphile. It is capable of disrupting negatively charged cell membranes and quenching the activity of adenosine triphosphate (ATP) synthase, leading to rapid cell death.<sup>[19,20]</sup> CTAB forms a bilayer structure on the surface of AuNRs and exists in dynamic equilibrium with the local environment, requiring toxic concentrations of free CTAB in the surrounding medium to maintain colloidal stability.<sup>[21,22]</sup> Considerable research output has been focused on either the passivation or replacement of this layer to render such particles safe for use in biomedical applications. Additionally, CTAB is a very poor stabilizing agent and fails to maintain the stability of particles in most biologically relevant buffers.<sup>[23]</sup> The human body presents a particularly challenging environment for the maintenance of colloidal stability, with human plasma exhibiting a relatively high salinity of around 300 mOsm L<sup>-1</sup> and contains a wide variety of biomolecules which will bind non-specifically to NPs, often undermining any specific surface functionalization bestowed on the particle. This is extremely problematic for most targeting strategies, as the

## 1. Introduction

The use of gold nanoparticles (AuNPs) in biomedical applications has grown to become one of the largest research areas in nanoscience.<sup>[1–4]</sup> Their strong plasmonic response and high photothermal efficiency have made them particularly appealing as photothermal conversion agents in the therapy and imaging

Dr. L. Roach, D. A. Paterson, D. V. B. Batchelor, Dr. S. C. T. Moorcroft, Dr. K. Critchley, Prof. S. D. Evans  
School of Physics and Astronomy  
University of Leeds  
Leeds LS2 9JT, UK  
E-mail: s.d.evans@leeds.ac.uk

Dr. M. E. Booth, Dr. N. Ingram, Dr. P. L. Coletta  
Leeds Institute for Medical Research  
Wellcome Trust Brenner Building  
St James's University Hospital  
Leeds LS9 7TF, UK

Prof. R. J. Bushby  
School of Chemistry  
University of Leeds  
Leeds LS2 9JT, UK

 The ORCID identification number(s) for the author(s) of this article can be found under <https://doi.org/10.1002/smll.202006797>.

© 2021 The Authors. Small published by Wiley-VCH GmbH. This is an open access article under the terms of the Creative Commons Attribution License, which permits use, distribution and reproduction in any medium, provided the original work is properly cited.

DOI: 10.1002/smll.202006797

resulting protein corona is typically 10–100 nm thick,<sup>[24]</sup> above the size of most targeting ligands (i.e., antibodies are ≈10–15 nm), leading to the corona completely obscuring such molecules.

Multiple functionalization strategies have been developed to combat these issues. The most common can be broadly grouped into two main categories: thiol displacement and surface passivation. Thiol displacement approaches rely on the high binding affinity between thiols and Au, leading to the competitive replacement of CTAB by molecules such as alkanethiols<sup>[25]</sup> or poly(ethylene glycol)-thiols (PEG-thiols).<sup>[26,27]</sup> Surface passivation focuses on encapsulating the CTAB in a low permeability polymer layer, such as poly(styrene sulfonate) (PSS)<sup>[12,28,29]</sup> or poly(acrylic acid),<sup>[30,31]</sup> or a layer of amorphous silica<sup>[32–37,47]</sup> thereby containing the CTAB and improving the biocompatibility.

An alternative approach to these is direct surfactant exchange. This method has received some attention in the literature, although remains relatively uncommon.<sup>[38–44]</sup> These techniques generally consist of dispersing a pellet of CTAB-functionalized AuNRs in a solution containing a large excess of the desired surfactant and then providing energy to encourage exchange between the solution and the particle surface in the form of heat or sonication. These techniques have been reported for several molecules including phospholipids<sup>[38–42]</sup> and oleate.<sup>[43,44]</sup> Phospholipids offer many benefits resulting from the highly tailorable properties of lipid membranes; including, low non-specific binding, high biocompatibility, the easy conjugation of targeting ligands and fluorophores, and the inclusion of steric-stabilizing agents such as PEG. Due to the twin alkyl chain structure of phospholipids, hydrophobic interactions between the molecules are increased compared with single-chain CTAB, hence phospholipid bilayers are more stable and thus suffer significantly less depletion to the surrounding solvent.<sup>[39]</sup> Phospholipids can be purchased relatively cheaply in bulk (≈0.23 \$ g<sup>-1</sup>) and the surfactant exchange procedure is straightforward, scalable, and reproducible.

This study focuses entirely on phospholipid exchange protocols, as oleate is too toxic to use for in vivo applications, having an intravenous median lethal dose (LD<sub>50</sub>) of 150 mg kg<sup>-1</sup> in mammals (by comparison CTAB is 44 mg kg<sup>-1</sup>).<sup>[45,46]</sup> Naturally occurring

phosphatidylcholines have an LD<sub>50</sub> above 10 000 mg kg<sup>-1</sup> and are widely considered nontoxic since they comprise 20–25% of cell membranes.<sup>[47,48]</sup>

Phospholipid-functionalized AuNRs were prepared following a protocol similar to that published by Matthews et al. for the preparation of dioleoylphosphatidylcholine (DOPC) – dioleoylphosphatidylglycerol (DOPG) functionalized AuNRs, which consists of resuspending and sonicating AuNRs in a solution containing phospholipid single unilamellar vesicles (SUVs) solution.<sup>[38]</sup> They reported that displacing with DOPC alone led to unstable AuNRs,<sup>[38]</sup> which disagrees with other studies utilizing phosphatidylcholines.<sup>[39,40,42,49]</sup> We found here that increasing the sonication time to ≈24 h and undergoing three rounds of displacement produced stable DOPC coated AuNRs. Consequently, the protocol was also made more reliable when scaling up to several hundred milliliters. Also, this protocol was found to work with both DOPC and DOPC – DOPG (19:1) mixtures. Additionally, it also allows the incorporation of PEGylated lipids, for which 95 mol% DOPC with 5 mol% distearoylphosphatidylethanolamine-methoxypoly(ethylene glycol) (DSPE-mPEG) was used, to provide additional steric stabilization, which produced similarly stable AuNRs.<sup>[50]</sup>

## 2. Results and Discussion

### 2.1. CTAB Replacement by Phospholipids

AuNRs were prepared using a seedless protocol utilizing a mixture of oleate and CTAB as stabilizers and shape-directing agents (**Figure 1**).<sup>[16]</sup> The concentrations of these agents were selected to produce AuNRs with a peak localized surface plasmon resonance (LSPR) wavelength of 811 nm, which provides low in vivo attenuation and optimized contrast for photoacoustic imaging in the first NIR biological window.<sup>[51]</sup> UV–vis spectra and TEM of the AuNRs are shown in **Figure 1a,b**, respectively. The mean dimensions of these AuNRs were a length of 57 nm and a diameter of 13.1 nm, with standard deviations of 7 and 1.2 nm, respectively, as determined from the TEM

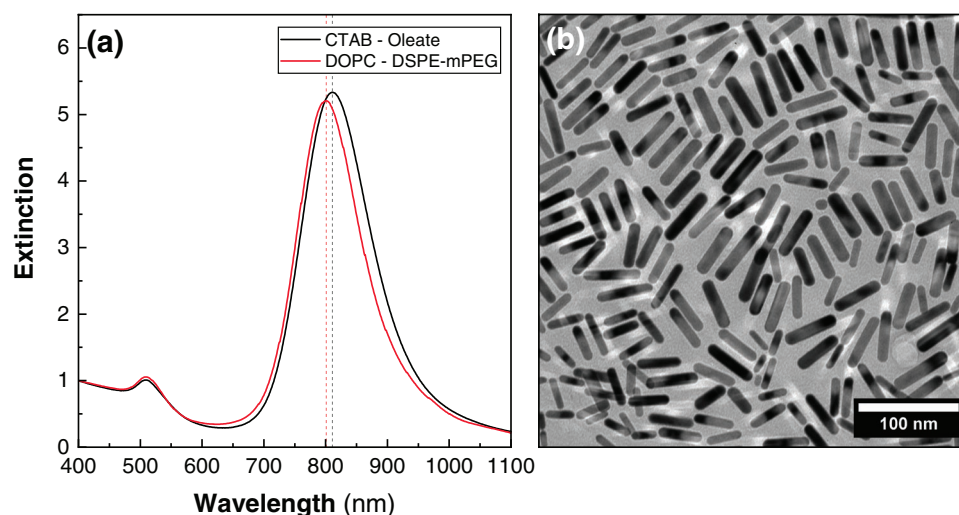


**Figure 1.** a) Spectra of AuNRs prepared for this study before and after phospholipid displacement. b) TEM image of the as-synthesized AuNRs.

measurements (Figure S1, Supporting Information). The CTAB – oleate coating was exchanged via resuspension in a DOPC – DSPE-mPEG (19:1) SUV solution for 24 h under sonication, repeated threefold, resulting in a slight blueshift of the LSPR to 801 nm with no indication of aggregation in spectrum. No change in morphology was observed as result of this exchange (Figure S2, Supporting Information). A lower sonication time of 4 h resulted in AuNRs which aggregated during centrifugation, a sonication time of 24 h produced AuNRs which could be repeatedly pelleted by centrifugation without loss of the AuNRs' plasmonic properties. After a single cycle of sonication, the  $\zeta$ -potential of DOPC AuNRs in 1 mM NaCl (pH 7) was measured to be positive ( $8 \pm 4$  mV), presumably due to the continued presence of CTAB (consistent with refs [39,42]). After the second cycle of displacement, the  $\zeta$ -potential was measured to be neutral. For biomedical applications, the maximum possible reduction of CTAB was a priority and a further round of phospholipid displacement was added to minimize the presence of residual CTAB. A sample of this batch was also coated with PSS to be used during in vitro and in vivo experiments. These particles were used for all tissue culture experiments and in vivo experiments, these particles were used for all further experiments unless otherwise stated. To assess the molecular species, which were present on the surface of the AuNRs after the

displacement,  $^1\text{H}$  NMR spectroscopy, surface enhanced Raman spectroscopy (SERS), and  $\zeta$ -potential measurements were used.

### 2.1.1. $^1\text{H}$ Nuclear Magnetic Resonance Spectroscopy

$^1\text{H}$  NMR spectroscopy was used to directly measure the chemical shifts of the ligands bound to the surface of both CTAB – oleate AuNRs and DOPC – DSPE-mPEG AuNRs. NMR spectroscopy of NP surface coatings is challenging due to both the small amount of material adhered to the particle surface and the long rotational tumbling time of nanoparticles compared to free molecules.<sup>[52]</sup> These combine to cause decreased signal intensity and broadened spectral peaks, which together to reduce the resolution of peaks. However, it is still possible to extract useful information about the molecular species present on the surface of the particles. The obtained spectra for the AuNRs are given in **Figure 2** along with the identified chemical shifts for each functionalization in **Tables 1** and **2**. The identification of the NMR peaks, for each molecule, is given in Section S5, Supporting Information. Before spectra collection, AuNRs were washed threefold by centrifugation and resuspended in  $\text{D}_2\text{O}$  to remove residual free lipid and CTAB. The CTAB – oleate AuNRs were kept as a pellet after the final centrifugation step and resuspended immediately

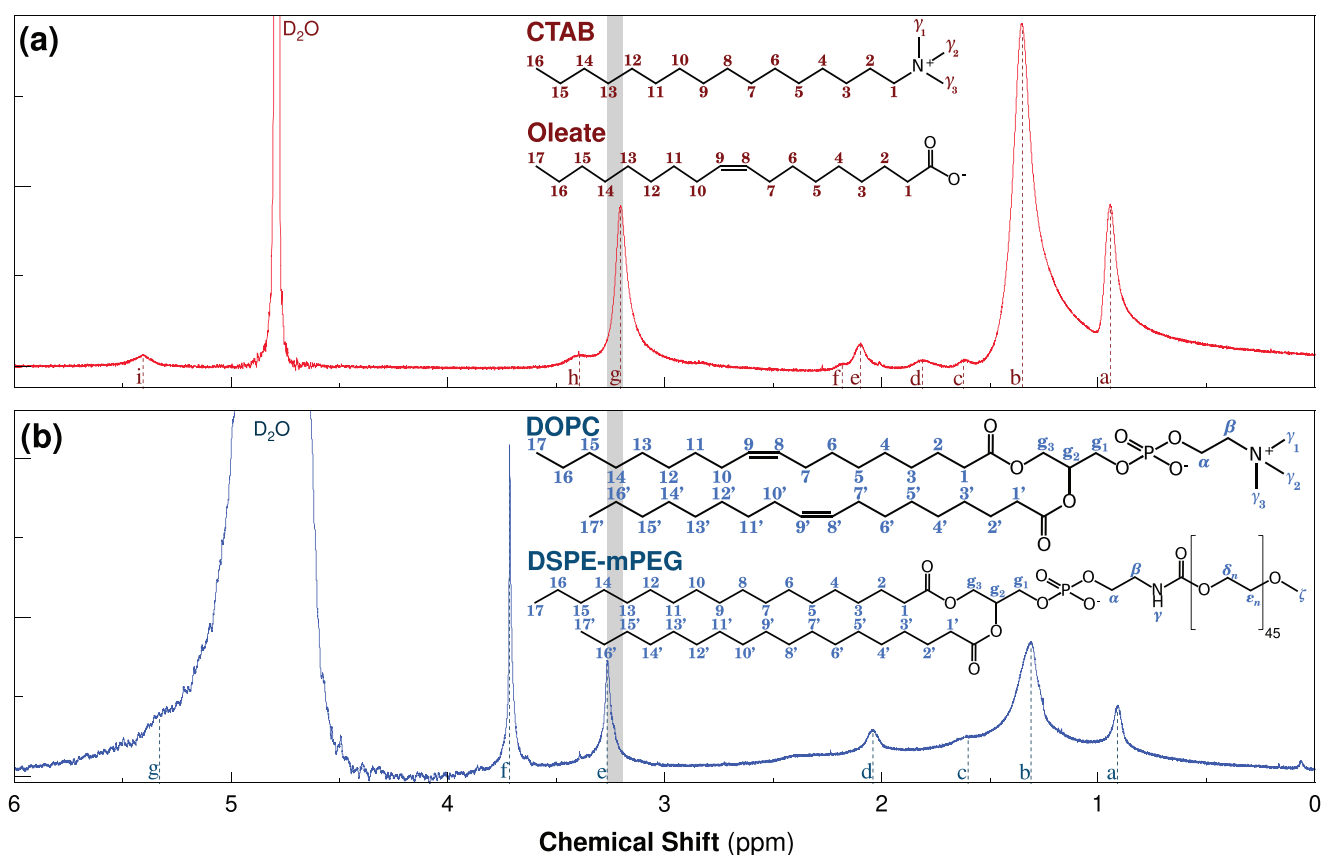


**Figure 2.**  $^1\text{H}$  NMR spectra for a)  $\approx 25$  nM CTAB – oleate (4:1) AuNRs and b)  $\approx 25$  nM DOPC – DSPE-mPEG (19:1) AuNRs. Chemical shift labels are given in Table 1. All spectra are taken in  $\text{D}_2\text{O}$ , details of sample preparation and acquisition settings for each spectrum are given in Section S5, Supporting Information. Inset in each figure are the molecular structures of a) CTAB and oleate, and b) DOPC and DSPE-mPEG. The spectra of solutions containing free CTAB, oleate, DOPC, and DOPG are given in Figure S4, Supporting Information. The grey band indicates the N-methyl protons of the trimethylammonium groups of interest.

**Table 1.** Chemical shift labels for the CTAB and NaOL AuNR  $^1\text{H}$  NMR spectrum given in Figure 2a.

Label	Chem. Shift [ppm]	Identification	
		CTAB	Oleate
a	0.94	16 ( $\text{CH}_3$ )	17 ( $\text{CH}_3$ )
b	1.35	3–15 ( $\text{CH}_2$ )	3–6, 11–16 ( $\text{CH}_2$ )
c	1.62	–	2 ( $\text{CH}_2$ )
d	1.81	2 ( $\text{CH}_2$ )	–
e	2.10	–	7, 10 ( $\text{CH}_2$ )
f	2.18	–	1 ( $\text{CH}_2$ )
g	3.20	$\gamma$ ( $\text{CH}_3$ )	–
h	3.39	1 ( $\text{CH}_2$ )	–
i	5.41	–	8, 9 (CH)

before spectra collection to avoid aggregation occurring due to CTAB depletion from the AuNR surface.

Figure 2a shows the spectrum obtained for CTAB – oleate AuNRs, the presence of CTAB and oleate can be inferred from the observed peaks (Figure S5a,b, Supporting Information). In particular, the asymmetric peaks at 0.94 and 1.36 ppm correlate well with the resonances of the  $-\text{CH}_3$  and  $-\text{[CH}_2\text{]}-$   $^1\text{H}$  nuclei of the aliphatic chains. Peaks at 2.10 and 5.41 ppm match the expected positions for  $^1\text{H}$  nuclei neighboring and within the alkene of the oleate chain, respectively. Shifts from the  $^1\text{H}$  nuclei located in the  $-\text{[CH}_2\text{]}-$  groups closest to the carboxylic acid head group of oleate are also visible at 1.62 and 2.18 (weak) ppm. Similarly, the protons from the equivalently positioned  $-\text{[CH}_2\text{]}-$  groups in CTAB can also be resolved in the spectrum at 1.81 and 3.39 ppm. A single peak associated with the *N*-methyl protons of CTAB can be observed at 3.20 ppm. These peaks suggest a mixed composition of CTAB and oleate present on the AuNR surface.

In the spectrum of the DOPC – DSPE-mPEG AuNRs (Figure 2b); peaks at 0.91, 1.31, and 1.60 (weak) ppm can be attributed to the aliphatic chains in both DOPC and DSPE-mPEG. Additionally, peaks at 2.04 and 5.33 (weak) ppm can be attributed to the alkenes in the chains of DOPC. The  $^1\text{H}$  resonances of the  $-\text{[CH}_2\text{]}-$  groups in the PEG chains of DSPE-mPEG are visible at 3.71 ppm. A single peak can be observed at 3.27 ppm associated with the *N*-methyl protons of DOPC. Combined these are consistent with a mixed composition of DOPC and DSPE-mPEG present on the surface of the AuNRs.

**Table 2.** Chemical shift labels for the DOPC – DSPE-mPEG AuNR  $^1\text{H}$  NMR spectrum given in Figure 2b.

Label	Chem. Shift [ppm]	Identification	
		DOPC	DSPE-mPEG
a	0.91	17, 17' ( $\text{CH}_3$ )	17, 17' ( $\text{CH}_3$ )
b	1.31	3–6, 11–16 ( $\text{CH}_2$ )	3–16 ( $\text{CH}_2$ )
		3'–6', 11'–16' ( $\text{CH}_2$ )	3'–16' ( $\text{CH}_2$ )
c	1.60	2, 2' ( $\text{CH}_2$ )	2, 2' ( $\text{CH}_2$ )
d	2.04	7, 10, 7', 10' ( $\text{CH}_2$ )	–
e	3.27	$\gamma$ ( $\text{CH}_3$ )	–
f	3.71	–	$\delta_n, \epsilon_n$ ( $\text{CH}_2$ )
g	(5.33)	8, 9, 8', 9' (CH)	–

The peaks of the aliphatic chains in CTAB, oleate, and the phospholipids broadly overlap. However, the peaks associated with the *N*-methyl protons of the CTAB and DOPC headgroups fall at different chemical shifts, 3.20 and 3.27 ppm respectively, and can be used as an identifier for the presence of CTAB. This difference in chemical shifts has previously been used by Orendorff et al. to demonstrate the removal of CTAB from the surface of palmitoylcholineglycerophosphocholine (POPC)-functionalized AuNRs.<sup>[39]</sup> In the spectrum of the DOPC – DSPE-mPEG AuNRs, the CTAB *N*-methyl proton peak (3.20 ppm) is not visible, there is instead only a single peak at 3.27 ppm. While complete elimination is impossible to conclude from the low signal-to-noise ratio of these measurements, they do suggest that substantial displacement of the CTAB from the surface of the AuNRs by phospholipids has occurred. However, this measurement on its own is limited and needs to be supported by additional characterization.

The chemical shift of the *N*-methyl protons of the AuNR-bound CTAB is lower than observed in free molecular CTAB solutions (Figure S5, Supporting Information). This has been reported elsewhere and is caused by a Knight shift due to the proximity of the group to the Au surface of the AuNR.<sup>[39,53,54]</sup> The value of 3.20 ppm seen here is also higher than seen for Au-bound CTAB elsewhere (i.e., 3.11 ppm,<sup>[39]</sup> 3.12 ppm,<sup>[53]</sup> and 3.16 ppm<sup>[54]</sup>), it is speculated that this may result from the inclusion of the negatively charged headgroup of oleate incorporated into the surface-bound CTAB bilayer, such changes in the chemical shifts have been observed in mixed micellar systems.<sup>[55]</sup> Regardless, it can still be resolved from the observed position of the DOPC *N*-methyl resonance at 3.27 ppm.

### 2.1.2. Surface-Enhanced Raman Spectroscopy

SERS was also used to identify the molecular species present on the surface of the phospholipid functionalized AuNRs. Post-phospholipid exchange AuNRs presented an LSPR peak wavelength of 801 nm (FWHM = 124 nm) close to the 785 nm wavelength of the laser, enabling a large field enhancement for SERS. The obtained spectra for the CTAB – oleate AuNRs and DOPC – DSPE-mPEG AuNRs are presented in Figure 3a,b, respectively.

To identify residual CTAB, the discussion here shall be restricted to the relevant features of the spectra. Firstly, a strong background signal can be seen in the spectrum of the DOPC – DSPE-mPEG (19:1) AuNRs making the spectrum appear to have a very uneven baseline. These originate from the PEG chains of DSPE-mPEG. These chains, being further from the Au surface, are less enhanced than other molecular groups, they comprise a large fraction of the surface coating and thus produce the observed background signal. The Raman spectra of PEG characteristically have strong bands resulting from overlapping peaks in the following regions 770–900, 1015–1170, 1230–1330, and 1410–1480  $\text{cm}^{-1}$ .<sup>[56]</sup> These bands have been marked in Figure 3b, and the various peaks which contribute to them are summarized in Table S2, Supporting Information.

The band at 176  $\text{cm}^{-1}$  has been attributed to the Au–Br<sup>−</sup> stretching mode ( $\nu(\text{Au–Br}^-)$ ) mode.<sup>[57]</sup> This peak is not present in pure CTAB and has been observed elsewhere to shift in AuNP solutions when the counter-ion is exchanged with other halide ions, such as chloride.<sup>[57]</sup> The presence of this peak

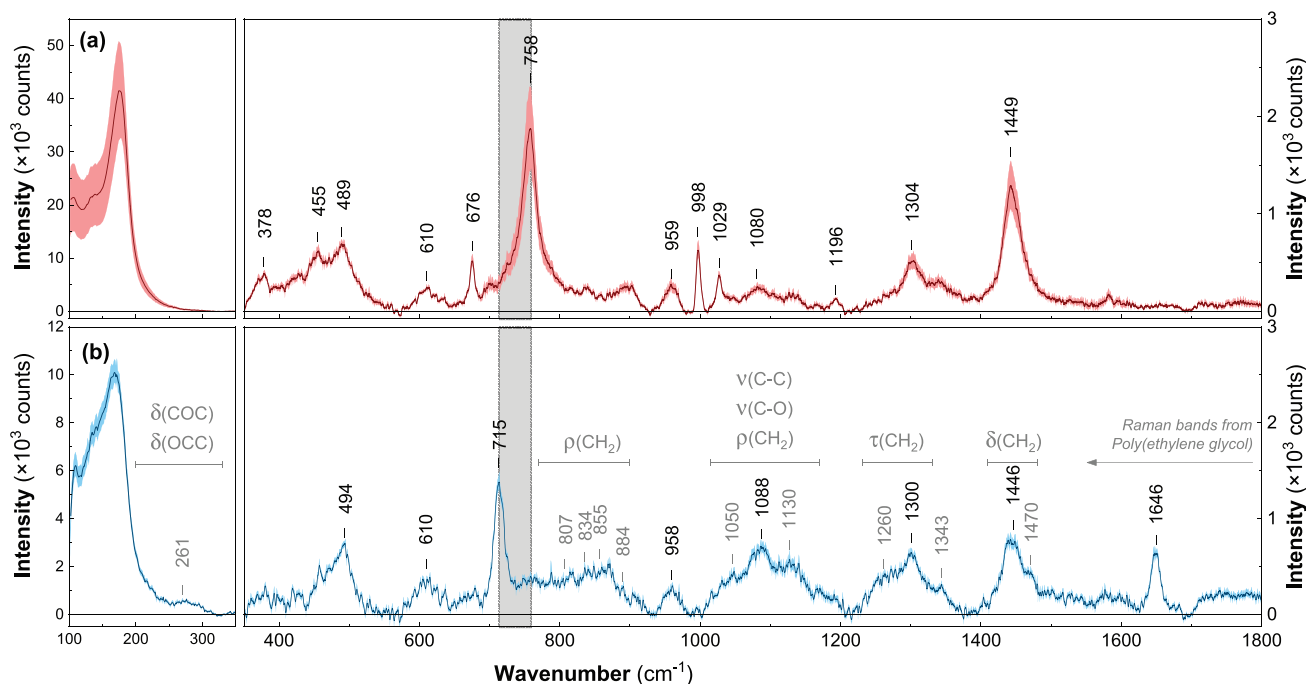


**Figure 3.** SERS spectra of AuNRs functionalized with a) CTAB – oleate (3:1), and b) DOPC – DSPE-mPEG (19:1). Peak positions have been annotated based on the identifications that are given in Tables S1 and S2, Supporting Information. In (b) strong bands are visible in the spectrum resulting from the broad overlapping peaks associated with the PEG chains of DSPE-mPEG. The regions occupied by these bands are marked in grey above the spectrum, the specific Stokes shifts associated to these have been marked on the spectrum itself in grey.

is not unexpected, as bromine forms a relatively strong polar covalent bond with the Au surface, and  $\text{AuBr}^-$  can bind to the trimethylammonium head groups of both phosphocholine and  $\text{CTA}^+$ . This bromide peak is thus expected to continue to be present, even after the exchange of the  $\text{CTA}^+$  and should enable the binding of phosphocholines to the Au surface. Indeed, this peak has been observed to remain in SERS studies by Matthews et al. of AuNRs coated by DOPC displacement of the CTAB lending further support to this conclusion.<sup>[38]</sup>

Two bands are of primary interest, firstly at  $763\text{ cm}^{-1}$  in the CTAB-oleate AuNR spectrum from the symmetric  $\nu(\text{C}_4\text{N}^+)$  mode, used widely as a diagnostic for the presence of CTAB on AuNPs (Figure 3a).<sup>[38,40,58,59]</sup> And secondly that at  $720\text{ cm}^{-1}$  in the DOPC – DSPE-mPEG AuNR spectrum associated with the symmetric  $\nu(\text{C}_4\text{N}^+)$  mode of the choline headgroup in DOPC (Figure 3b). Despite both these modes originating from a trimethylammonium group, the proximity of the strongly electronegative oxygen in the choline of DOPC leads to a lower wavenumber peak. The absence of a peak at  $768\text{ cm}^{-1}$  in the DOPC-DSPE-mPEG AuNR spectrum implies that the CTAB population on the surface of the AuNRs has been reduced below the threshold of detection. Whilst it is possible to say that the majority of the CTAB has been removed, a lower limit is difficult to determine by this technique.

### 2.1.3. $\zeta$ -Potential

Finally, to complement the characterization of the AuNR surface coatings, a pH-dependent  $\zeta$ -potential study was undertaken before and after the exchange of the CTAB with phospholipid.

To allow the identification of residual CTAB on the AuNRs, a single batch was prepared without the presence of oleate (Figure S6, Supporting Information). These CTAB-only AuNRs present a positive charge at all pH values (Figure 4a), this is consistent with the behavior expected for CTAB. The measured value of  $\zeta = (20.4 \pm 0.7)\text{ mV}$ , reflects the depletion of the surface-bound CTAB due to repeated washing by centrifugation. The surface charge presented by the CTAB coating is dependent on the concentration of free CTAB in the suspending medium and the dynamic equilibrium between this and surface-bound CTAB.<sup>[22]</sup>

By comparison, AuNRs prepared using a mixture of 38 mM CTAB and 12 mM oleate yield a  $\zeta$ -potential which is pH-dependent (Figure 4a). The  $\zeta$ -potential is positive at all pH values consistent with a higher surface concentration of  $\text{CTA}^+$  than oleate<sup>-</sup>. However, the presence of the negatively charged oleate ions in the surface coating has substantially suppressed the  $\zeta$ -potential ( $\approx 12\text{ mV}$  for  $\text{pH} > 7$ ). Although the reported  $\text{pK}_a$  for a free oleate molecule is 5.0, the surface-bound oleate here presents an apparent  $\text{pK}_a$  of 4.3 due to it being packed amongst an excess of positively charged trimethylammonium headgroups. This leads to localized repulsion of cations in the vicinity of the water/bilayer interface and a localized pH shift of  $\approx 0.7$ .<sup>[60,61]</sup>

AuNRs which have undergone exchange with DOPC also show a pH-dependent  $\zeta$ -potential (Figure 4b). This results from the zwitterionic character of DOPC; it is neutrally charged at physiological pH and above but presents a positive charge for pH values  $< 5$ . The phosphate group in the free DOPC molecule has a  $\text{pK}_a$  of 1.88, but this shifts to around  $\text{pH} \approx 1$  when the molecule is embedded in a bilayer.<sup>[62]</sup> The DOPC AuNRs follow

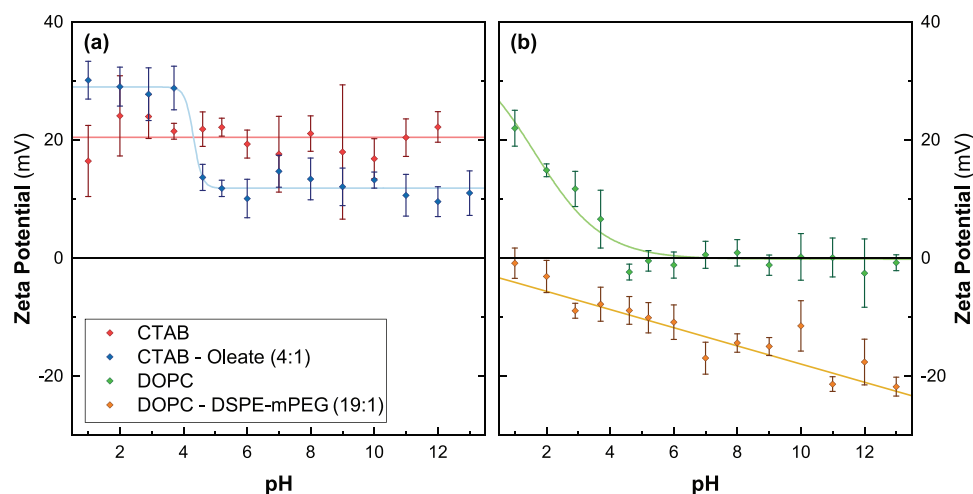


**Figure 4.** Experimentally determined  $\zeta$ -potentials for AuNRs coated with a) CTAB, & CTAB – oleate (4:1), and b) DOPC, & DOPC – DSPE-mPEG (19:1) as a function of buffer pH ( $C_{\text{ion}} = 10 \text{ mM}$ ).

this behavior, but the effective  $pK_a$  of the AuNR-bound lipids cannot be reliably determined, because it requires measurement at a pH where all phosphate groups are protonated (i.e.,  $< \text{pH } 0$ ), which was not practical to work at. The pH response is significantly broadened, which has been observed elsewhere for PC lipids bound to nanoparticles.<sup>[39]</sup>

Notably, the DOPC AuNRs have a  $\zeta$ -potential of  $\approx 0 \text{ mV}$  above pH 5 (to within error) consistent with the removal of positively-charged  $\text{CTA}^+$  from the AuNR surface. Previously reported  $\zeta$ -potentials for AuNRs functionalized by phosphatidylcholines still display some positive charge at high pH, implying the continued presence of  $\text{CTA}^+$ .<sup>[39,41,42]</sup> Comparatively, neutral surface potential (to within  $\pm 3 \text{ mV}$ ) was observed suggesting the additional rounds of sonication in phospholipid SUV solution deployed here are effective at removing this residual CTAB from the surface coating.

Finally, the measurements were repeated on AuNRs coated with a 19:1 mixture of DOPC and DSPE-mPEG (Figure 4b). Whilst the phosphate groups of DOPC and DSPE-mPEG both have  $pK_a$  values of around 1.8, they should not have an apparent effect on the pH response of particles functionalized with a significant number of PEGylated phospholipids. Since  $\zeta$ -potential measurements are only sensitive to the functional groups exposed at the surface of the particle, the extended PEG brush structure should effectively screen the pH response of the phosphate and trimethylammonium groups present on these molecules. It was therefore expected, based on the protonation dynamics of PEG, that the particles would present a neutral  $\zeta$ -potential at all pH. This was not observed, instead, the particles displayed a slightly negative  $\zeta$ -potential at low pH, which grows increasingly negative with increasing pH, this behavior has been observed elsewhere (e.g., refs. <sup>[63,64]</sup>). This can likely be explained by the preferential absorption of anionic species onto the PEG, which has been observed to occur for oligo(ethylene glycol) monolayers.<sup>[65]</sup>

The observed shifts in  $\zeta$ -potential are consistent with the known  $pK_a$  values of the molecules that functionalize the AuNRs in this study. The absence of any positive charge on the DOPC-functionalized AuNRs implies that the level of

CTAB on the surface of the AuNRs was successfully reduced to trace levels during the phospholipid exchange process described above. This was supported by the NMR and Raman spectroscopy. In all cases, the presence of CTAB was not detectable by any technique in the phospholipid-functionalized AuNR samples implying its displacement to near-zero levels.

## 2.2. Stability in Biologically Relevant Media

While stability in biologically relevant media has been assessed for more common AuNR coatings such as CTAB and PSS, the stability of phospholipid-coated AuNRs outside of the undemanding environment of deionized water has received no attention.<sup>[40,42,48,66]</sup> The stability of our AuNRs was explored in a variety of “biologically relevant media”, such as buffers, cell culture medium (CCM), serum, and plasma. Three buffers were selected as surrogates to test the impact of similar ion concentrations to those seen in human plasma on the stability of AuNPs. Two commercially available buffers were used, Dulbecco’s phosphate-buffered saline (DPBS) and Plasma-Lyte 148 (PL-148), an isotonic intravenously administered fluid replacement with physiological pH and balanced electrolyte component. These buffers are optimized for cell culture and rapid intravenous metabolism, respectively. Thirdly, a bespoke buffer was prepared to closely match the homeostatic concentrations of the most common electrolytes in human plasma ( $C_{\text{ion}} \geq 1 \text{ mM}$ ) dubbed “pseudo-plasma” buffer (PP). In addition to these electrolyte mixtures, mixtures of RPMI 1640 CCM and fetal bovine serum (FBS) were also used. Because FBS is heat-treated to remove the fibrinogen and coagulant protein content, murine plasma containing these proteins was also tested. This represents the closest possible match to the *in vivo* models in which these particles will be tested. A detailed breakdown of the electrolyte profiles and biomolecule content of these media is provided in Section S8, Supporting Information. Aggregation is readily seen in the UV-vis spectra as a broadening and shift in the peak wavelength of the LSPR bands. Spectra were taken

over 2 weeks, presented in their entirety in Section S8.1–S8.7, Supporting Information, a few selected examples are presented in Figure 5.

The stability of CTAB AuNRs was assessed by two parallel experiments. AuNRs were washed threefold and suspended in the media of interest and additionally with the same media including an additional 1 mM CTAB. This made it possible to distinguish between aggregation induced by the degradation of the CTAB bilayer and charge screening due to ions in solution. The effect of this was easily visible in the results, DPBS, PL148, and PP buffers containing washed CTAB AuNRs show aggregation at 96, 197, and 188 mOsm L<sup>-1</sup> respectively. When 1 mM CTAB was included alongside the particles, these

concentrations at which they became unstable increased to 193, 197, and 282 mOsm L<sup>-1</sup> respectively. CTAB AuNRs were unstable in all CCM + FBS combinations, but the presence of 1 mM CTAB significantly increased their stability. CTAB appears to be a poor stabilization agent under biological conditions, although this is somewhat immaterial given its high cytotoxicity.

PSS is often considered a good moiety with which to provide strong charge stabilization to AuNPs.<sup>[67,68]</sup> However, here PSS AuNRs were observed to aggregate at 289, 198, and 94 mOsm L<sup>-1</sup> in DPBS, PL148, and PP, respectively. Faster and more complete aggregation was observed above these concentrations. PSS-coated AuNRs were also unstable in CCM. This

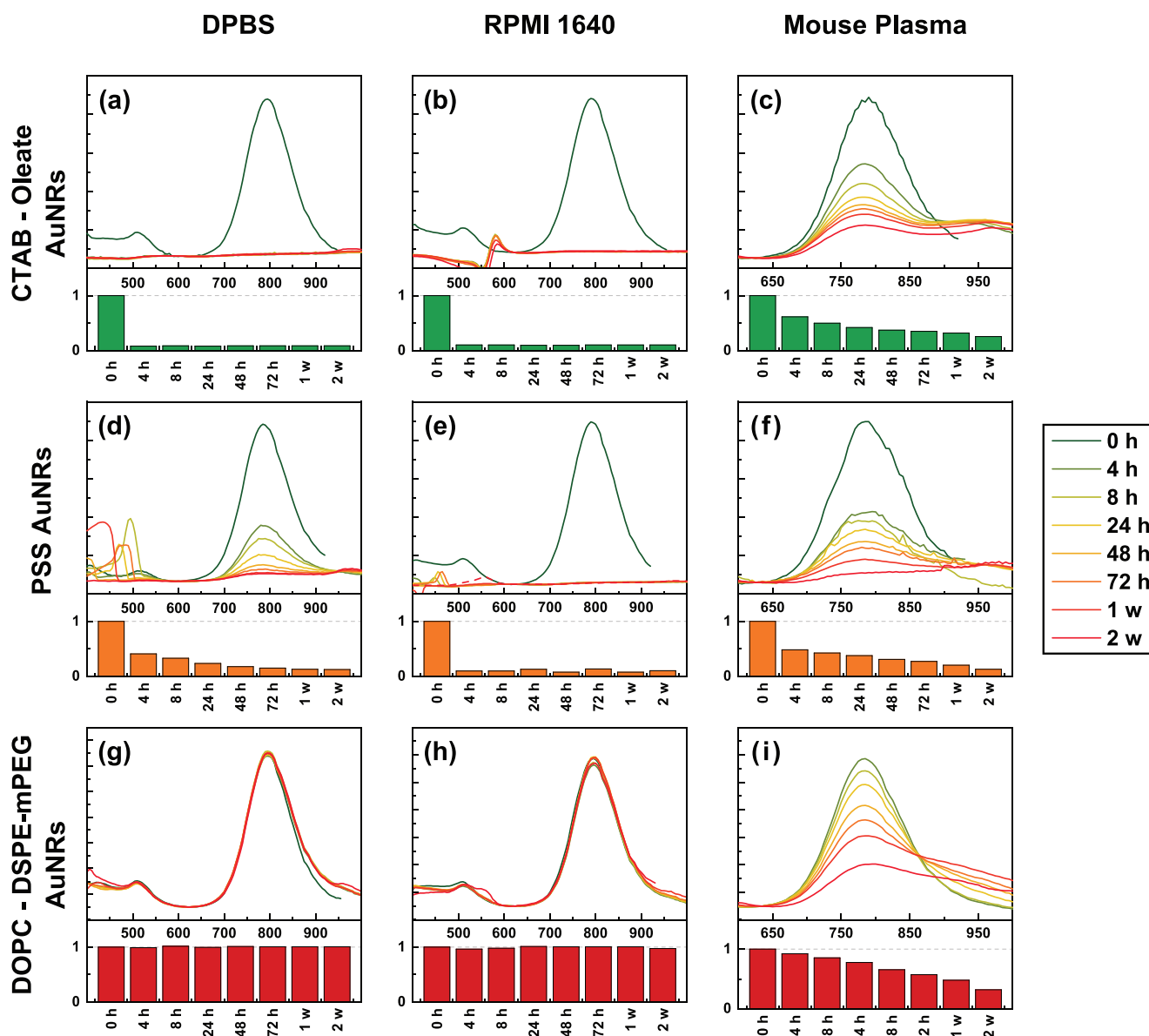


**Figure 5.** Absorbance spectra of AuNRs during stability testing over 2 weeks. a–c) CTAB – oleate, d–f) PSS, and g–i) DOPC – DSPE-mPEG functionalized AuNRs in (a,d,g) DPBS, (b,e,h) RPMI 1640 cell culture media, and (c,f,i) mouse plasma. The top section of each panel shows a series of UV-vis spectra of each experimental condition at different time points over 2 weeks. The lower panel shows the magnitude of the LSPR (normalized to  $t = 0$ ) as a function of time. A full summary of the stability data under all conditions is given in Section S8, Supporting Information.

has been observed previously, where the presence of serum proteins was required to maintain stability.<sup>[69]</sup> The particles here were not stable in 10% FBS-enriched CCM, however other studies have observed PSS AuNRs to be stable under these conditions (i.e., refs. <sup>[12,69]</sup>). Increasing the serum content further did provide stability and PSS-functionalized AuNRs show good stability in 50% and 100% serum, suggesting corona formation can stabilize the particles, consistent with these other results.

The PSS AuNRs aggregate at a faster rate than CTAB – oleate AuNRs in mouse plasma. Throughout the experiment the LSPR decreased to the point of being virtually undetectable, accompanied by an increase in the extinction at higher wavelengths consistent with the formation of aggregates.

No aggregation was visible in the spectra of DOPC – DSPE-mPEG in any of the buffers, in CCM, or in serum. The optical properties were consistent across all concentrations and time points. Some aggregation was observed in mouse plasma. The intensity of the LSPR is around 80% of its initial value after 24 h, which is still high enough to be utilized for photothermal therapy, suggesting they are stable enough for in vivo application. DOPC – DSPE-mPEG AuNRs outperformed CTAB – oleate and PSS AuNRs in all buffers, CCM + FBS combinations, and mouse plasma. This improved stability results from the zwitterionic character of DOPC and the additional steric stabilization from the PEG chains of DSPE-mPEG. Both stabilization mechanisms do not rely on electrostatic repulsion and hence are significantly better at maintaining NP stability under highly saline conditions.

All coatings performed considerably worse in mouse plasma compared with FBS, likely resulting from non-specific interactions between the AuNRs and the fibrinogen/coagulant proteins absent in FBS. If it is the presence of fibrinogen and coagulant proteins that are the cause of this increased instability, it could have important implications for the applications of nanoparticles in vivo and may warrant further investigation.

### 2.3. In Vitro Studies

To ensure that the particles were not inherently toxic to mammalian cells after CTAB displacement, and therefore suitable for in vivo use; the cytotoxicity of the DOPC – DSPE-mPEG AuNRs was assessed on four cell lines; SW620 human colorectal adenocarcinoma, HEK293 human embryonic kidney, HCT116 human colorectal adenocarcinoma, and LS174T colorectal adenocarcinoma. Viabilities were compared against those seen for PSS AuNRs, a commonly used biocompatible surface functionalization.<sup>[12,29,69,70]</sup>

The results of the cell viability assays are presented in **Figure 6a,b**. In all cases, the cell incubated with DOPC – DSPE-mPEG AuNRs showed higher cell viabilities than their PSS-coated equivalents after 24 h co-incubation. For three cell lines, SW620, HCT116, and LS174T, ≈100% cell viability was seen even at the highest dose administered of 200 μg mL<sup>-1</sup>. HEK293 cells showed some toxicity, reaching 50% viability at (55 ± 1) μg mL<sup>-1</sup>, by comparison when treated with PSS AuNRs this viability was found for dose levels over 10× higher (4 ± 1) μg mL<sup>-1</sup>. The half maximal inhibitory concentration (IC<sub>50</sub>) for the SW620, HCT116, and LS174T cells treated with PSS-AuNRs were (102 ± 1), (186 ± 1), and (81 ± 1) μg mL<sup>-1</sup>, respectively.

Previous studies of the cytotoxicity of phospholipid AuNRs are limited to two papers. The first in HeLa cells used phosphatidylcholine-functionalized AuNRs up to concentrations of 2.9 μg mL<sup>-1</sup> and reported 20% cell death (which seems likely to be due to high residual levels of CTAB).<sup>[41]</sup> The second using dimyristoylglycerophosphocholine (DMPC)-functionalized AuNRs measured cell viabilities up to 20 μg mL<sup>-1</sup> in MCF-7 and HMEC-1 cells, with no drop off in viability.<sup>[40]</sup> These are both significantly below the doses presented here. From our results, the IC<sub>50</sub> has been determined to be over 200 μg mL<sup>-1</sup>, for the three cell lines studied here, this is an excessively high dose compared with the concentrations likely to be achieved in vivo.

To demonstrate that this low toxicity did not originate from minimal levels of cellular uptake, cells treated with the particles were studied by optical and electron microscopy. An optical darkfield image of cells incubated with 40 μg mL<sup>-1</sup> AuNRs for 6 h is presented in **Figure 6c**. Large numbers of AuNRs can be observed as bright spots within the interior of the cells. The number and intensity of these spots were observed to correlate strongly with the dose of AuNRs administered (see additional darkfield images in Section S9, Supporting Information). TEM of cell sections shows that the AuNRs were intracellular (**Figure 6d**). Based on cell staining, it appears that these particles are contained within endosomes, consistent with the expected endocytotic uptake route of most nanomaterials.<sup>[71]</sup> These particles appear to be highly biocompatible at the concentrations expected to be achieved in vivo.

Another concern relating to the use of nanoparticles in vivo is that of hemolysis, the rupture or destruction of red blood cells. This is a particular concern for AuNPs functionalized with a positively charged amphiphile such as CTAB, which can disrupt cellular membranes.<sup>[19]</sup> CTAB, PSS, and DOPC – DSPE-mPEG AuNRs were assessed for their potential to cause hemolysis. The results of this assay are shown in **Figure 7a**. CTAB AuNRs showed high levels of lysis at both 100 μg and 20 μg mL<sup>-1</sup> (73% and 37% respectively). Additionally, the supernatant (SN) extracted from the 100 μg mL<sup>-1</sup> CTAB sample showed similar levels of lysis (41%) to that of the 20 μg mL<sup>-1</sup> sample. This is consistent with the membrane disruption expected from dissociated CTAB in solution.<sup>[19,20]</sup>

By comparison, the lysed fraction following exposure to the SN from both the PSS- and DOPC – DSPE-mPEG AuNRs was low (1% and 2% respectively). Similarly, at a concentration of 20 μg mL<sup>-1</sup>, low levels of lysis were seen for both the PSS- (3%) and DOPC – DSPE-mPEG AuNRs (2%). However, DOPC – DSPE-mPEG AuNRs performed better at 100 μg mL<sup>-1</sup> with a lysed fraction of 8%, compared to the 24% seen using PSS AuNRs at the same concentration.

The photothermal heat generation of these AuNRs was measured at a range of concentrations and continuous wave (CW) laser fluences were measured (**Figure S9**, Supporting Information). The AuNRs synthesized here have a molar extinction coefficient of 5.4 × 10<sup>9</sup> M<sup>-1</sup> cm<sup>-1</sup> at 811 nm and are therefore extremely efficient photothermal conversion agents. A local temperature increase above body temperature of ≈10 °C is required to achieve cell death over short exposure times.<sup>[5]</sup> This temperature increase was achieved at concentrations >50 μg mL<sup>-1</sup> at 0.32 W cm<sup>-2</sup> (**Figure S9a**, Supporting Information). This fluence is notable as it represents the

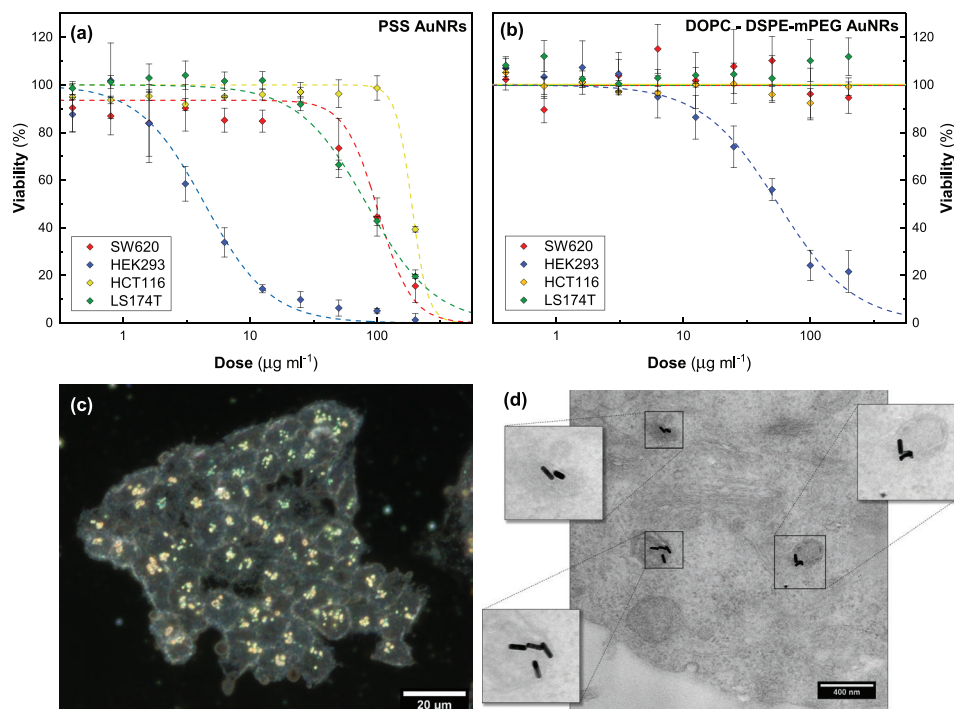


**Figure 6.** In vitro cell viabilities of SW620, HEK293, HCT116, and LS174T cells after 24 h incubation with AuNRs. Cells incubated with increasing concentrations of a) PSS-AuNRs and b) DOPC – DSPE-mPEG (19:1) AuNRs. Results are expressed as a percentage of the control plates ( $0 \mu\text{g mL}^{-1}$ ) and are the mean result from three plates at different passage numbers. Results are fitted with a Hill-type dose–response curve. From these fits the  $\text{IC}_{50}$  of the PSS AuNRs are determined to be  $(102 \pm 1)$ ,  $(4 \pm 1)$ ,  $(186 \pm 1)$ , and  $(81 \pm 1) \mu\text{g mL}^{-1}$  for the SW620, HEK293, HCT116, and LS174T cell lines, respectively. The DOPC – DSPE-mPEG AuNRs show  $\approx 100\%$  cell viability at all concentrations measured in the SW620, HCT116, and LS174T cell-lines, so no  $\text{IC}_{50}$  is determined. For HEK293 cells it is determined to be  $(55 \pm 1) \mu\text{g mL}^{-1}$  significantly better than the equivalent test with PSS AuNRs. c) Darkfield microscopy image of SW620 cells incubated with  $40 \mu\text{g mL}^{-1}$  DOPC – DSPE-mPEG (19:1) AuNRs for 6 h before fixing. d) TEM image of a section through an SW620 cell incubated for 4 h before fixing. AuNRs can be seen to have been taken up into endosomes as denoted by the darker circular structures shown in the magnified inserts.

maximum permissible exposure (MPE) at 811 nm as stated by ANSI standard.<sup>[72]</sup> Utilizing fluences above the MPE, temperature increases of 10, 23, and 58 °C, at 1, 2, and 3  $\text{W cm}^{-2}$  respectively, were achieved at concentrations as low as  $5 \mu\text{g mL}^{-1}$  (Figure S9c–f, Supporting Information). Hence these particles are demonstrably suitable for application as photothermal conversion agents.

The photothermal stability of the AuNRs was also assessed by extended exposure to a CW laser source, which is also a potential issue due to the possibility of particle reshaping. The particles showed no discernible change in the extinction spectrum and heat generation after a single 10 min exposure at  $3 \text{W cm}^{-2}$  (Figure S11a, Supporting Information). The AuNRs were quite resilient over repeated exposure cycles (a single cycle being 10 min at  $3 \text{W cm}^{-2}$  followed by 20 min at  $0 \text{W cm}^{-2}$ ). After 60 cycles (6 h cumulative exposure), the maximum temperature generated only dropped by  $\approx 4\%$ . This is a relatively small drop and well beyond any exposure time that would be encountered during treatment, consequently, these AuNRs should be well suited to therapeutic applications using CW light sources (Figure S11b,c, Supporting Information). At the termination of the experiment (160 cycles,  $>26 \text{h}$  cumulative exposure) this had dropped by 25% (Figure S11d, Supporting Information). The changes observed here are consistent with the thermal reshaping observed in heated solutions of AuNRs.<sup>[73,74,75]</sup> At the

maximum temperatures seen here ( $\approx 70 \text{ °C}$ ), these reshaping processes occur over hours and should not affect photothermal therapy using such particles.

To demonstrate the efficacy of this temperature increase in killing cancerous cells, the particles were incubated with SW620 colorectal adenocarcinoma cells at  $20 \mu\text{g mL}^{-1}$  for 4 h and subsequently exposed to an intensity of  $1 \text{W cm}^{-2}$ , at 801 nm for a range of exposure times. Cell viability was reduced to  $\approx 30\%$  after 2.5 min and near-complete cell death was observed after 5 min (Figure 7b). Cell exposure to the laser in the absence of AuNRs resulted in no drop in viability.

#### 2.4. In Vivo Studies

Following on from the in vitro studies, murine models were used to assess the in vivo toxicity and biodistribution of our AuNRs. Immediately following intravenous injection there were no visible signs of distress or irritation and no weight loss or abnormal behaviors were observed during the following 9 d in any of the animals. All mice survived post-injection to the planned time of sacrifice. This further supports the conclusion that these particles demonstrate good biocompatibility, and are well tolerated in the murine model, in agreement with the in vitro experiments above.

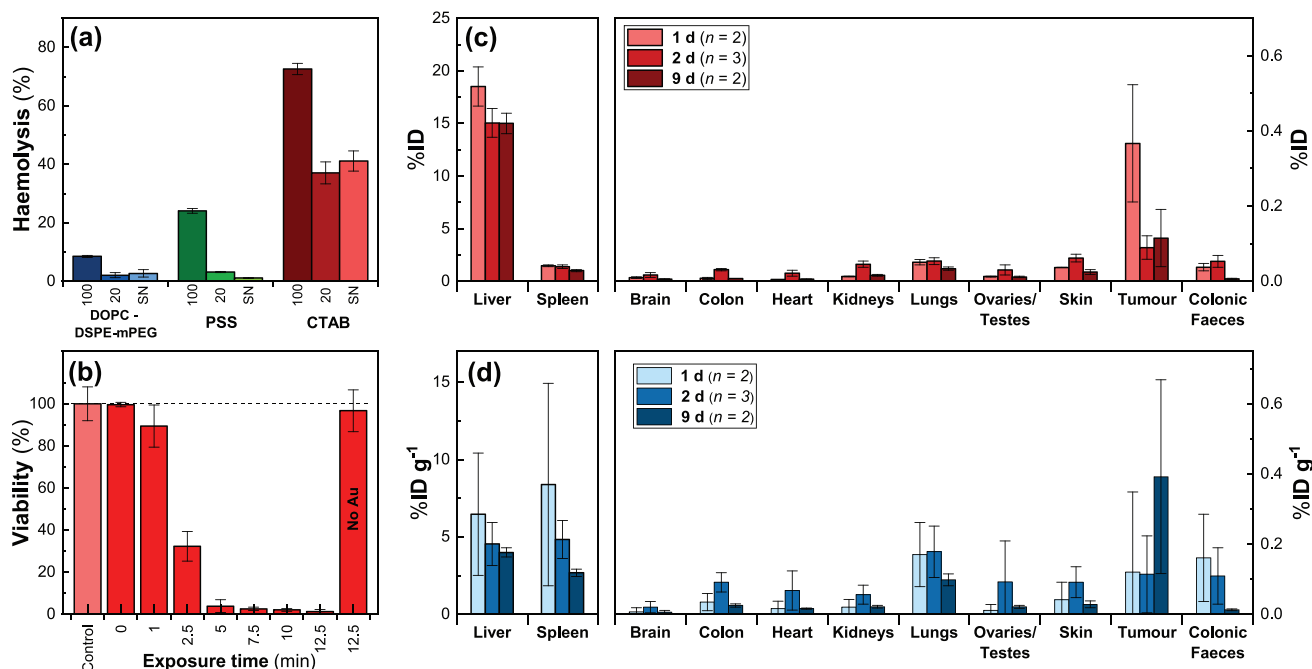


**Figure 7.** a) Measured hemolysis fractions for DOPC – DSPE-mPEG, PSS, and CTAB -oleate AuNRs at 100  $\mu\text{g mL}^{-1}$  and 20  $\mu\text{g mL}^{-1}$ . The lysis values for the supernatant (SN) extracted from a 100  $\mu\text{g mL}^{-1}$  samples are also presented. b) Viabilities of SW620 cells exposed to 1 W  $\text{cm}^{-2}$  CW light. Cells are incubated with 20  $\mu\text{g mL}^{-1}$  DOPC – DSPE-mPEG AuNRs for 4 h before illumination. Cell viability assays are repeated in triplicate and are expressed as a percentage of the control viability (no Au, no laser exposure). c) Measured Au concentrations in mice treated with DOPC – DSPE-mPEG AuNRs in each of the tested tissues expressed as a percentage of the injected dose (%ID). d) The same %ID values expressed per gram of dry tissue sample (%ID $\text{g}^{-1}$ ). Note: a larger vertical scale has been used for the liver and spleen to that of all other organs.

Biodistribution studies were undertaken to determine the *in vivo* fate of the phospholipid AuNRs in tumor-bearing mice. This was achieved by *ex vivo* inductively coupled plasma mass spectrometry (ICP-MS) analysis of the organs of the injected mice harvested 1, 2, and 9 d post-injection. It was expected that the tissues which would show the highest uptake were the liver and spleen due to clearance by the mononuclear phagocyte system (MPS), and elimination via the hepatobiliary route.<sup>[76]</sup> The results of this study expressed as a fraction of the injected dose (%ID) are presented in Figure 7b. Most of the sample was found in the liver ( $\approx 15\%$ ), however, when the mass of the digested tissue (%ID per gram of tissue, %ID $\text{g}^{-1}$ ) is accounted for, the density of Au within the spleen is similar to that seen within the liver (Figure 7c). This distribution is consistent with reported biodistribution values for PEGylated particles more generally.<sup>[77–80]</sup>

The concentrations of these particles in the liver and spleen can be seen to decrease with time, likely due to the particles being cleared by the MPS. Au was still detectable in the liver and spleen after 9 d, paired with the observation of relatively low quantities of Au in the colonic feces, suggesting a relatively low rate of elimination. Further experiments are required to fully characterize the timescale over which these particles are eliminated by the body. Although some studies of PEGylated particles have detected particles in the liver and spleen 15 months after the administration of the original AuNPs, indicating that complete elimination may never be achieved.<sup>[81]</sup> However, in most cases, there are no reports of long-term toxicity emerging from this continued presence. It remains an open question whether the persistence of such particles *in vivo* should be tolerated as part of any treatment.

Only a very small proportion of the injected dose was observed in the subcutaneous tumor ( $(0.4 \pm 0.2)\%$ ,  $(0.1 \pm 0.03)\%$ , and  $(0.1 \pm 0.08)\%$  at 1 d, 2 d, and 9 d, respectively), therefore the particles did not preferentially accumulate here, or any accumulation occurred over a different timescale compared to the chosen time points. Modification of the particles with active targeting could potentially increase the uptake of these particles within the tumor especially with the recent finding by Sindhwani et al. that 97% of AuNP entry to tumors is via an active rather than passive mechanism.<sup>[82]</sup>

No residual Au is seen in any of the other organs, the %ID measured for the brain, colon, heart, kidneys, lungs, sex organs, and skin are all close to the detection limit for our samples in the ICP-MS. This is expected but also indicates that DOPC – DSPE-mPEG functionalized AuNRs are not being retained because of some unknown interaction resulting from the surface functionalization in any of the other major organs.

### 3. Conclusion

This work demonstrates that the displacement of CTAB with a variety of phospholipids can be achieved through repeated rounds of sonication and cleaning through centrifugation. This repeated process appears to be more effective at removing CTAB from the surface of AuNRs than other published methods, producing no detectable CTAB when characterized by NMR spectroscopy, SERS, and  $\zeta$  potential measurements.

Furthermore, these particles present superior stability compared with the other surface functionalizations tested here in a variety of biologically relevant media. In vitro models showed very high levels of biocompatibility and are well tolerated by murine models when administered in vivo. They have high photothermal conversion efficiencies, achieving high temperatures when illuminated by NIR light that are capable of rapidly inducing cell death in cancerous cells. They do, however, appear to have a relatively low rate of clearance from the liver and spleen, which warrants further investigation over a longer timescale.

Thus, phospholipid coated AuNRs represent a promising avenue for further cancer nanomedicine research and should be highly effective in applications such as plasmonic photothermal therapy and photoacoustic imaging. The method presented here is highly robust and can be utilized with a wide range of phospholipids, enabling highly tailorable surface properties to be achieved in a straightforward and cost-effective protocol.

#### 4. Experimental Section

Details of the materials used, and experimental methods can be found in the Supporting Information (Sections S1 and S2, respectively). All animal procedures were approved by the UK Home Office and carried out according to the Animals (Scientific Procedures) Act 1986 and under the project license of Dr. P. Louise Coletta (70/7965) with all work involving the handling of live animals was performed by Dr. Nicola Ingram under PIL IDD6965FF.

#### Supporting Information

Supporting Information is available from the Wiley Online Library or from the author.

#### Acknowledgements

L.R. would like to thank the University of Leeds for the award of a Ph.D. studentship through the University Research Scholarship. M.E.B. would like to thank the National Institute of Health Research for funding as an Academic Clinical Fellow at the University of Leeds. N.I. and P.L.C. express gratitude to the EPSRC for funding through grants EPSRC EP/1000623/1 and EP/P023266/1. P.L.C. would also like to thank the EPSRC for grant EP/S001069/1. D.A.P., S.D.E., and R.J.B. thank the EPSRC for financial support (EP/P024041/1). D.V.B.B. thanks K. de Silva for support through the provision of an Alumni Ph.D. scholarship. K.C. thanks the EPSRC for financial support (EP/P005233/1 and EP/T013753/1). S.D.E. would also like to thank the EPSRC for financial support (EP/P023266/1 and EP/P00122X/1). S.D.E. is supported by the National Institute for Health Research (NIHR) infrastructure at Leeds. The views expressed are those of the author(s) and not necessarily those of the National Health Service (NHS), the NIHR or the Department of Health. The authors would like to thank Mr. Joe Fox for his assistance in providing TEM microscopy at short notice.

#### Conflict of Interest

The authors declare no conflict of interest.

#### Data Availability Statement

The dataset associated with this paper is available from the University of Leeds Data Repository and is located at <https://doi.org/10.5518/922>.

#### Keywords

biocompatibility, gold nanorods, in vivo, phospholipids, stability

Received: October 30, 2020

Revised: February 2, 2021

Published online: March 8, 2021

- [1] N. S. Abadeer, C. J. Murphy, *J. Phys. Chem. C* **2016**, *120*, 4691.
- [2] L. A. Austin, M. A. Mackey, E. C. Dreaden, M. A. El-Sayed, *Arch. Toxicol.* **2014**, *88*, 1391.
- [3] X. Huang, M. A. El-Sayed, *J. Adv. Res.* **2010**, *1*, 13.
- [4] S. Jain, D. G. Hirst, J. M. O'Sullivan, *Br. J. Radiol.* **2012**, *85*, 101.
- [5] D. Jaque, L. Martínez Maestro, B. del Rosal, P. Haro-Gonzalez, A. Benayas, J. K. Plaza, E. Martín Rodríguez, E. Gracia Solé, *Nanoscale* **2014**, *6*, 9494.
- [6] R. S. Riley, E. S. Day, *Wiley Interdiscip. Rev.: Nanomed. Nanobio-technol.* **2017**, *9*, e1449.
- [7] J. Weber, P. C. Beard, S. E. Bohndiek, *Nat. Methods* **2016**, *13*, 639.
- [8] S. C. T. Moorcroft, L. Roach, D. G. Jayne, Z. Y. Ong, S. D. Evans, *ACS Appl. Mater. Interfaces* **2020**, *12*, 24544.
- [9] R. Vankayala, C. C. Lin, P. Kalluru, C. S. Chiang, K. C. Hwang, *Biomaterials* **2014**, *35*, 5527.
- [10] L. Wang, Y. Yuan, S. Lin, J. Huang, J. Dai, Q. Jiang, D. Cheng, X. Shuai, *Biomaterials* **2016**, *78*, 40.
- [11] S. Ye, S. D. Connell, J. R. McLaughlan, L. Roach, Z. Aslam, N. Chankhunthod, A. P. Brown, R. Brydson, R. J. Bushby, K. Critchley, P. L. Coletta, A. Markham, S. D. Evans, *Adv. Funct. Mater.* **2020**, *30*, 2003512.
- [12] S. Ye, G. Marston, J. R. McLaughlan, D. O. Sigle, N. Ingram, S. Freear, J. J. Baumberg, R. J. Bushby, A. F. Markham, K. Critchley, P. L. Coletta, S. D. Evans, *Adv. Funct. Mater.* **2015**, *25*, 2117.
- [13] S. Ye, A. A. Azad, J. E. Chambers, A. J. Beckett, L. Roach, S. C. T. Moorcroft, Z. Aslam, I. A. Prior, A. F. Markham, L. P. Coletta, S. J. Marciniak, S. D. Evans, *Small* **2020**, *16*, 2003793.
- [14] A. R. Rastinehad, H. Ansatos, E. Wajswol, J. S. Winoker, J. P. Sfakianos, S. K. Doppalapudi, M. R. Carrick, C. J. Knauer, B. Taouli, S. C. Lewis, A. K. Tewari, J. A. Schwartz, S. E. Canfield, A. K. George, J. L. West, N. J. Halas, *Proc. Natl. Acad. Sci. U. S. A.* **2019**, *116*, 18590.
- [15] P. K. Jain, K. S. Lee, I. H. El-Sayed, M. A. El-Sayed, *J. Phys. Chem. B* **2001**, *11*, 7238.
- [16] L. Roach, S. Ye, S. C. T. Moorcroft, K. Critchley, P. L. Coletta, S. D. Evans, *Nanotechnology* **2018**, *29*, 135601.
- [17] X. Ye, L. Jin, H. Caglayan, J. Chen, G. Xing, C. Zheng, V. Doan-Nguyen, Y. Kang, N. Engheta, C. R. Kagan, C. B. Murray, *ACS Nano* **2012**, *6*, 2804.
- [18] A. Sánchez-Iglesias, N. Winckelmans, T. Altantzis, S. Bals, M. Grzelczak, L. M. Liz-Marzán, *J. Am. Chem. Soc.* **2017**, *139*, 107.
- [19] I. P. Lau, H. Chen, J. Wang, H. C. Ong, K. C.-F. Leung, H. P. Ho, S. K. Kong, *Nanotoxicology* **2012**, *6*, 847.
- [20] D. Schnacter, *Ph.D. Thesis*, The State University of New Jersey **2013**.
- [21] B. Nikoobakht, M. A. El-Sayed, *Langmuir* **2001**, *17*, 6368.
- [22] B. C. Rostro-Kohanloo, L. R. Bickford, C. M. Payne, E. S. Day, L. J. E. Anderson, M. Zhong, S. Lee, K. M. Mayer, T. Zal, L. Adam,

- C. P. N. Dinney, R. A. Drezek, J. L. West, J. H. Hafner, *Nanotechnology* **2009**, *20*, 434005.
- [23] H. C. Huang, B. Barua, D. B. Kay, K. Rege, *ACS Nano* **2009**, *3*, 2941.
- [24] E. Koglin, E. Tarazona, S. Kreisig, M. Schwuger, *Colloids Surf. A* **1997**, *123–124*, 523.
- [25] J. Casas, M. Venkataramasubramani, Y. Wang, L. Tang, *Biosens. Bioelectron.* **2013**, *49*, 525.
- [26] F. Schulz, W. Friedrich, K. Hoppe, T. Vossmeier, H. Weller, H. Lange, *Nanoscale* **2016**, *8*, 7296.
- [27] Z. Zhang, M. Lin, *RSC Adv.* **2014**, *4*, 17760.
- [28] A. Gole, C. J. Murphy, *Chem. Mater.* **2005**, *17*, 1325.
- [29] A. P. Leonov, J. Zheng, J. D. Clogston, S. T. Stern, A. K. Patri, A. Wei, *ACS Nano* **2008**, *2*, 2481.
- [30] J. W. Hotchkiss, A. B. Lowe, S. G. Boyes, *Chem. Mater.* **2007**, *19*, 6.
- [31] J. W. Hotchkiss, B. G. R. Mohr, S. G. Boyes, *J. Nanopart. Res.* **2010**, *12*, 915.
- [32] C. L. Bayer, Y.-S. Chen, S. Kim, S. Mallidi, K. Sokolov, S. Emelianov, *Biomed. Opt. Express* **2011**, *2*, 1828.
- [33] L.-C. Chen, C.-W. Wei, J. S. Souris, S.-H. Cheng, C.-T. Chen, C.-S. Yang, P.-C. Li, L.-W. Lo, *J. Biomed. Opt.* **2010**, *15*, 016010.
- [34] W.-H. Chen, C.-X. Yang, W.-X. Qiu, G.-F. Luo, H.-Z. Jia, Q. Lei, X.-Y. Wang, G. Liu, R.-X. Zhuo, X.-Z. Zhang, *Adv. Healthcare Mater.* **2015**, *4*, 2247.
- [35] J. V. Jokerst, M. Thangaraj, P. J. Kempen, R. Sinclair, S. S. Gambhir, *ACS Nano* **2012**, *6*, 5920.
- [36] G. P. Luke, A. Bashyam, K. A. Homan, S. Makhija, Y. S. Chen, S. Y. Emelianov, *Nanotechnology* **2013**, *24*, 455101.
- [37] J. Comenge, O. Fragueiro, J. Sharkey, A. Taylor, M. Held, N. C. Burton, B. K. Park, B. Wilm, P. Murray, M. Brust, R. Lévy, *ACS Nano* **2016**, *10*, 7106.
- [38] J. R. Matthews, C. M. Payne, J. H. Hafner, *Langmuir* **2015**, *31*, 9893.
- [39] C. J. Orendorff, T. Alam, D. Y. Sasaki, B. C. Bunker, J. A. Voigt, *ACS Nano* **2009**, *3*, 971.
- [40] P. B. Santhosh, N. Thomas, S. Sudhakar, A. Chadha, E. Mani, *Phys. Chem. Chem. Phys.* **2017**, *19*, 18494.
- [41] H. Takahashi, Y. Niidome, T. Niidome, K. Keneko, H. Kawasaki, S. Yamada, *Langmuir* **2006**, *22*, 2.
- [42] J.-H. Yoo, H. S. Han, C. Lee, K.-P. Yoo, T. Kang, *J. Nanosci. Nanotechnol.* **2013**, *13*, 7239.
- [43] Z. Li, S. Tang, B. Wang, Y. Li, H. Huang, H. Wang, P. Li, C. Li, P. K. Chu, X.-F. Yu, *ACS Biomater. Sci. Eng.* **2016**, *2*, 789.
- [44] J. Wang, H. Huang, D. Zhang, M. Chen, Y. Zhang, X. Yu, L. Zhou, Q. Wang, *Nano Res.* **2015**, *8*, 2548.
- [45] *Safety Data Sheet - Cetyltrimethylammonium Bromide, MSDS No. 278833*, Santa Cruz Biotechnology, Inc., Dallas, TX **2011**.
- [46] *Safety Data Sheet - Sodium Oleate, MSDS No. O0057; TCI Europe N.V.: Zwijndrecht, Netherlands* **2018**.
- [47] H. Aldewachi, T. Chalati, M. N. Woodroffe, N. Bricklebank, B. Sharrack, P. Gardiner, *Nanoscale* **2018**, *10*, 19.
- [48] A. Werlein, A. Peters, R. Ngoune, R. K. Winkler, G. Pütz, *Biochim. Biophys. Acta, Biomembr.* **2015**, *1848*, 1599.
- [49] E. T. Castellana, R. Gamez, R. D. H. Russell, *J. Am. Chem. Soc.* **2011**, *133*, 4182.
- [50] R. Abou-Saleh, M. Swain, S. D. Evans, N. Thomson, *Langmuir* **2014**, *30*, 5557.
- [51] M. J. Duffy, O. Planas, A. Faust, T. Vogl, S. Hermann, M. Schäfers, S. Noneli, C. A. Strassert, *Photoacoustics* **2018**, *9*, 49.
- [52] L. E. Marbella, J. E. Millstone, *Chem. Mater.* **2015**, *27*, 2721.
- [53] F. Hubert, F. Testard, O. Spalla, *Langmuir* **2008**, *24*, 9219.
- [54] Z. M. Sui, X. Chen, L. Y. Wang, L. M. Xu, W. C. Zhang, W. C. Chai, C. J. Yang, *Phys. E* **2006**, *33*, 308.
- [55] J. Hao, R. Lu, H. Wang, S. Dong, *J. Dispersion Sci. Technol.* **1997**, *18*, 379.
- [56] J. L. Koenig, A. C. Angood, *J. Polym. Sci., Part A-2* **1970**, *8*, 1787.
- [57] S. Lee, L. J. E. Anderson, C. M. Payne, J. H. Hafner, *Langmuir* **2011**, *27*, 14748.
- [58] Y. Li, J.-Z. Xu, L. Zhu, H. Xu, M.-W. Pan, G.-J. Zhong, Z.-M. Li, *Polymer* **2014**, *55*, 4765.
- [59] M. Tebbe, C. Kuttner, M. Männel, A. Fery, M. Chanana, *ACS Appl. Mater. Interfaces* **2015**, *7*, 5984.
- [60] S. Yamaguchi, K. Bhattacharyya, T. Tahara, *J. Phys. Chem. C* **2011**, *115*, 4168.
- [61] S. Salentinig, L. Sagalowicz, O. Glatter, *Langmuir* **2010**, *26*, 11670.
- [62] D. Marsh, *Handbook of Lipid Bilayers*, CRC Press, Boca Raton **2013**.
- [63] F. Meng, G. H. M. Engbers, J. Feuen, *J. Biomed. Mater. Res., Part A* **2004**, *70A*, 49.
- [64] M. Bloemen, W. Brullot, T. T. Luong, N. Geukens, A. Gils, T. Verbiest, *J. Nanopart. Res.* **2012**, *14*, 1100.
- [65] H. J. Kreuzer, R. L. Wang, M. Grunze, *J. Am. Chem. Soc.* **2003**, *125*, 8384.
- [66] C. J. Orendorff, C. J. Murphy, *J. Phys. Chem. B* **2006**, *110*, 3990.
- [67] X. Hu, X. Gao, *Phys. Chem. Chem. Phys.* **2011**, *13*, 10028.
- [68] Z. Shi, W. Ren, A. Gong, X. Zhao, Y. Zou, E. M. B. Brown, X. Chen, A. Wu, *Biomaterials* **2014**, *35*, 7058.
- [69] R. G. Rayavarapu, W. Petersen, L. Hartsuiker, P. Chin, H. Janssen, F. W. van Leeuwen, C. Otto, S. Manohar, T. G. van Leeuwen, *Nanotechnology* **2010**, *21*, 145101.
- [70] W. Pissuwan, Y. Kumagai, N. I. Smith, *Part. Part. Syst. Charact.* **2013**, *30*, 427.
- [71] L. Kou, J. Sun, Y. Zhai, Z. He, *Asian J. Pharm. Sci.* **2013**, *8*, 1.
- [72] *ANSI Z136.1 American National Standard for Safe use of Lasers*, Standard, American Laser Institute, Orlando, FL **2014**.
- [73] K. C. Ng, W. Cheng, *Nanotechnology* **2012**, *23*, 105602.
- [74] A. B. Taylor, A. M. Siddiquee, J. W. M. Chon, *ACS Nano* **2014**, *8*, 12071.
- [75] Z. Zou, Q. Zhang, Q. Zhao, F. Peng, H. Wang, H. Yu, J. Yang, *Colloids Surf. A* **2010**, *372*, 177.
- [76] D. van Haute, J. M. Berlin, *Ther. Delivery* **2017**, *8*, 763.
- [77] Y. Akiyama, T. Mori, Y. Katayama, N. Takuro, *J. Controlled Release* **2009**, *139*, 81.
- [78] H. Gao, J. Liu, C. Yang, T. Cheng, L. Chu, H. Xu, A. Meng, S. Fan, L. Shi, J. Liu, *Int. J. Nanomed.* **2013**, *8*, 4229.
- [79] T. Niidome, M. Yamagata, Y. Okamoto, Y. Akiyama, H. Takahashi, T. Kawano, Y. Katayama, Y. Niidome, *J. Controlled Release* **2006**, *114*, 343.
- [80] J. S. Suk, Q. Xu, N. Kim, J. Hanes, L. M. Ensign, *Adv. Drug Delivery Rev.* **2016**, *99A*, 28.
- [81] M. R. K. Ali, M. Rahman, Y. Wu, T. Han, X. Peng, M. A. Mackey, D. Wang, H. J. Shin, Z. G. Chen, H. Xiao, R. Wu, Y. Tang, D. M. Shin, M. A. El-Sayed, *Proc. Natl. Acad. Sci. U. S. A.* **2017**, *114*, E3110.
- [82] S. Sindhvani, A. M. Syed, J. Ngai, B. R. Kingston, L. Maiorino, J. Rothschild, P. MacMillan, Y. R. N. U. Zhang, T. Hoang, J. L. Y. Wu, S. Wilhelm, A. Zilman, S. Gadde, A. Sulaiman, B. Ouyang, Z. Lin, L. Wang, M. Egeblad, W. C. W. Warren, *Nat. Mater.* **2020**, *19*, 566.